.

Optimising Urban Measurement Networks for CO_2 Flux Estimation: A High-Resolution Observing System Simulation Experiment using GRAMM/GRAL

Sanam N. Vardag[1,2,*] and Robert Maiwald[1,*]

[1]Institut für Umweltphysik, Universität Heidelberg, Im Neuenheimer Feld 229, 69120 Heidelberg
[2]Heidelberg Center for the Environment, Universität Heidelberg, Im Neuenheimer Feld 229, 69120 Heidelberg
[*]These authors contributed equally to this work.

Correspondence: Sanam N. Vardag (sanam.vardag@uni-heidelberg.de)

Abstract. To design a monitoring network for estimating CO_2 fluxes in an urban area, a high-resolution Observing System Simulation Experiment (OSSE) is performed using the transport model Graz Mesoscale Model (GRAMMv19.1) coupled to the Graz Lagrangian Model (GRALv19.1). First, a high-resolution anthropogenic emission inventory, which is considered as the truth serves as input to the model to simulate CO_2 concentration in the urban atmosphere on 10 m horizontal resolution in a 12.3 km x 12.3 km domain centered in Heidelberg, Germany. By sampling the CO_2 concentration at selected stations and feeding the measurements into a Bayesian inverse framework, CO_2 fluxes on neighbourhood scale are estimated. Different configurations of possible measurement networks are tested to assess the precision of posterior CO_2 fluxes. We determine the trade-off of between quality and quantity of sensors by comparing the information content for different set-ups. Decisions on investing in a larger number or more precise sensors can be based on this result. We further analyse optimal sensor locations for flux estimation using a Monte Carlo approach. We examine the benefit of additionally measuring carbon monoxide. We find that including CO as tracer in the inversion allows the disaggregation of different emission sectors such as traffic emissions. Finally, we quantify the benefit of introducing a temporal correlation into the prior emissions. The results of this study give implications for an optimal measurement network design for a city like Heidelberg. The study showcases the general usefulness of the developed inverse framework using GRAMM/GRAL for planning and evaluating measurement networks in an urban area.

1 Introduction

Urban areas and cities play a crucial role in mitigating climate change. A large share of greenhouse gases (about 70 % of anthropogenic CO_2 emissions) is emitted in urban areas offering a huge potential to reduce greenhouse gas emissions (World Bank, 2010). To realise the full mitigation potential and to verify any emission reductions, solid knowledge of local greenhouse

gas emissions is required. In addition to inventory-based ("bottom-up") emission estimates, measurements of greenhouse gases in an urban network can be used in an inverse framework to quantify emissions ("top-down"). In a top-down approach, concentration measurements are linked to total fluxes using an atmospheric transport model. Information from the measurements together with prior emission information are combined in an inversion to minimise differences in measurements and forward transported concentrations under consideration of the associated uncertainties. The result is the so-called posterior emission estimate. In the last years, many city CO_2 monitoring networks have formed at the local level. Monitoring systems in urban areas can be found in the San Francisco Bay Area (Turner et al., 2016; Delaria et al., 2021), Indianapolis (Turnbull et al., 2019; Oda et al., 2017; Lauvaux et al., 2016; Turnbull et al., 2015; Richardson et al., 2017; Deng et al., 2017; Davis et al., 2017; Balashov et al., 2020; Miles et al., 2021), Salt Lake City (Mallia et al., 2020; Kunik et al., 2019), Davos (Lauvaux et al., 2013), and Paris (Lian et al., 2022; Wu et al., 2016; Bréon et al., 2015). In future, it is expected that more networks will be installed supporting local mitigation endeavors (Jungmann et al., 2022). In order to optimise the investment in a measurement network and maximise the knowledge gained from these measurements, several parameters need to be considered preferably in the design-phase. These parameters include the number and location of nodes, the uncertainty of the measurements, and the co-measured species. They need to be optimised under consideration of a limited financial budget.

Observing System Simulation Experiments (OSSEs) offer a valuable tool for assessing different monitoring networks and estimating the benefits they provide for flux estimation. In an OSSE, all parameters are known, and instead of using actual measurements, pseudo observations are employed in the inversion process. These pseudo observations represent simulated concentrations based on emission inventories, which are assumed to be true. In the following, we refer to these as true emissions. The true emissions are transported in the atmosphere using a model. Uncertainties of measurements and model transport may be included to represent a realistic setting. Analysis of the posterior emissions, and in particular, the comparison of flux estimations derived from pseudo observations with the true emissions, allows an evaluation of the potential of the pseudo observations for flux estimation. This enables analysis of different measurement network designs in OSSEs, facilitating the identification of optimal network configurations and providing insights into the inversion set-up characteristics. For instance, Turner et al. (2016) conducted an experiment using the actual sensor locations of the BEACON measurement network in the San Francisco Bay Area to assess the trade-off between low-cost sensors in higher quantities and less, but more expensive sensors with higher accuracy, by comparing the error in flux estimates for various set-ups. Their findings revealed two types of measurement network configurations: noise-limited configurations, where the inversion improves more substantially with higher sensor quality, and site-limited configurations, where the improvement is greater with an increased number of sensors. While Turner et al. (2016) selected the sensor locations randomly from a fixed set of sensor locations, another study by Mano et al. (2022) developed an algorithm to determine optimal sensor locations for a measurement network. This algorithm utilises the entropy of expected trace gas concentration to identify ideal measurement positions. Alternatively, Thompson and Pisso (2023) applied a Monte Carlo approach to optimise sensor locations. They were able to pinpoint from a set of possible sites which are most valuable for CH_4 flux estimation on a European scale. Thus, performing measurements at the selected sites improves the posterior emission estimates.

Further, the CO_2 estimate may benefit from measuring co-emitted trace gases. For example, carbon monoxide (CO) is emitted alongside fossil fuel combustion. The CO/CO_2 ratios varies with emission sectors and regions, which makes it potentially useful as a proxy for CO_2 emissions from fossil fuel combustion in general, and more specifically as a tracer for traffic emissions (Vogel et al., 2010). Nathan et al. (2018) quantitatively analysed the advantages of CO as a trace gas in the inversion
60 set-up using the INFLUX measurement network in Indianapolis. By incorporating CO measurements in the inversion, Nathan et al. (2018) successfully distinguished spatially overlapping sources into two sectors. Furthermore, the uncertainty of prior fluxes significantly affects the inversion process. Kunik et al. (2019) conducted an OSSE using a measurement network in Salt Lake City to examine the influence of the prior flux uncertainty. They demonstrated that incorporating realistic correleations in the prior between fluxes in the temporal and spatial dimensions can substantially improve the inversion results. Wu et al. (2018)
65 obtained similar results regarding spatial correlation in the city of Indianapolis. These examples highlight the possibilities of OSSEs in analyzing urban network monitoring and consider various aspects and site-specific characteristics. The resolution of urban OSSEs usually is 1 km or coarser and limited by the large computation time of the transport model, as well as of the inversion on a high resolution.

In our study, we employ the Reynolds-Averaged Navier Stokes model Graz Mesoscale Model (GRAMM) coupled to the Graz
70 Lagrangian Model (GRAL) as a forward model (GRAMM/GRAL). This model assumes hourly steady-state conditions and simulates a 10 m x 10 m concentration field at five heights per emission group within a 12.3 km x 12.3 km domain, accounting for the flow around buildings. This high resolution exceeds the typical 1 km resolution of previous OSSEs, enabling the use of any 10 m x 10 m grid cell as pseudo measurement data for inversion, thus keeping the aggregation errors small. The high resolution is possible due to the comparatively cheap forward model when using the catalogue approach (see Sect. 2), as
75 well as due to the hourly steady state assumption of the model such that the Jacobian required for the inversion can be easily determined (see Sect. 2.2). This property allows for network optimization considering many different parameters and locations, including those affected by street channeling and surrounding buildings. Specifically, our study focuses on analysing sensor quantity versus quality, sensor location optimisation, the use of CO as an additional tracer, and the temporal correlation of the prior for the first time on high-resolution of 10 m x 10 m within a 150 km^2 domain centered around Heidelberg. With these first
80 experiments, we seek to showcase the ability of the framework in general.

2 Methodology

2.1 The atmospheric transport model GRAMM/GRAL

Emissions and concentrations are linked via the atmospheric transport. Modelling the atmospheric transport is a challenging task due to the high complexity of the turbulence. Especially for heterogenic urban environments, models need to account
85 for different land use types and their associated properties, flow around buildings, and topography, which influence the atmospheric transport. For this task, there are two types of models, which are commonly used and which attempt to solve the Navier Stokes equation: Large Eddy Simulations (LES) and Reynolds-averaged Navier-Stokes simulations (RANS). While LES models handle this by explicitly solving large turbulent structures and parametrising small turbulent structures, RANS models use

temporal averaging to reduce the complexity of the problem and generate steady-state flow fields. The model GRAMM/GRAL
90 is a RANS model. RANS models are computationally cheaper compared to LES models (Blocken, 2018). GRAMM/GRAL
consists of the two models GRAMM and GRAL which can also be used separately. Description of the model can be found in
Berchet et al. (2017a, b), as well as in Öttl (2020). The model assumes hourly steady-state conditions and takes into account
the flow around buildings.

GRAMM is a prognostic mesoscale model (Oettl, 2021) which computes hourly quasi steady state wind fields from synoptic
95 forcing given parameters associated to land use cover such as surface roughness or thermal conductivity, and for a given topogra-
phy of the domain. The synoptic forcing is determined by wind direction, wind speed, and a stability class to parameterise the
turbulence. In this study, we chose a domain size of 20 km x 20 km centered in Heidelberg, Germany with a resolution of 100 m
x 100 m. GRAL uses the GRAMM wind fields as mesoscale input and refines the wind fields to a higher resolution taking into
account the flow around buildings. The GRAL domain size is 12.3 km x 12.3 km with a resolution of 10 m x 10 m. The vertical
100 resolution of the wind field is 2 m with a total of 200 cells. The domain borders for GRAMM and GRAL are shown in Fig.
1. A Lagrangian particle simulation is performed to obtain the hourly steady state particle distribution from emissions, which
is used to compute the concentration field. The emission types can be point, line, and area sources which can be grouped into
up to 99 emission groups. An emission group is a set of emissions, which is stored and optimised together. For each emission
group a concentration field can be obtained.

105 In this study, the computational costs are further reduced by utilizing a catalogue approach. The catalogue approach is based
on the fact that for longer periods similar weather situations reoccur. Utilizing the repetition of similar weather conditions a
catalogue of wind fields is computed covering all typical prevailing wind situations for the area. For Heidelberg, we use 1008
synoptic forcings, which are stored and are hourly matched with wind measurements to provide wind fields for the considered
period. In particular, during the matching measured and pre-calculated simulated wind speeds and directions are compared
110 hourly to find the pre-calculated wind situation that minimised the difference to measurements for that hour. Details can be
found in Berchet et al. (2017a, b).

As the lifetime of CO_2 is much larger than the period of interest, the concentration enhancement of CO_2 in the atmosphere is
proportional to the magnitude of the emissions. Using this linearity, a pre-computed concentration field can be scaled linearly to
account for a change in the emissions. Emissions from an emission group can be scaled accounting for e.g. different temporal
115 profiles. Note that emission groups do not have to be homogeneous, but may have a sub-structure. However, scaling the
emission group then means scaling all emissions in their sub-structure. The total concentration enhancement field is obtained
as a linear combination of the concentration fields for each emission group. The choice of the emission groups should reflect
the relative variability of the emissions sources such that grouped emissions should have a high correlation. The division into
emission groups is described in Sec. 2.4.

120 **2.2 The inverse framework**

In this study, the inverse problem is estimating emissions x (vector of length m) from the forward modelled concentration
measurements y (vector of length n). The relation between the measurements and the state vectors, i.e. emission groups is
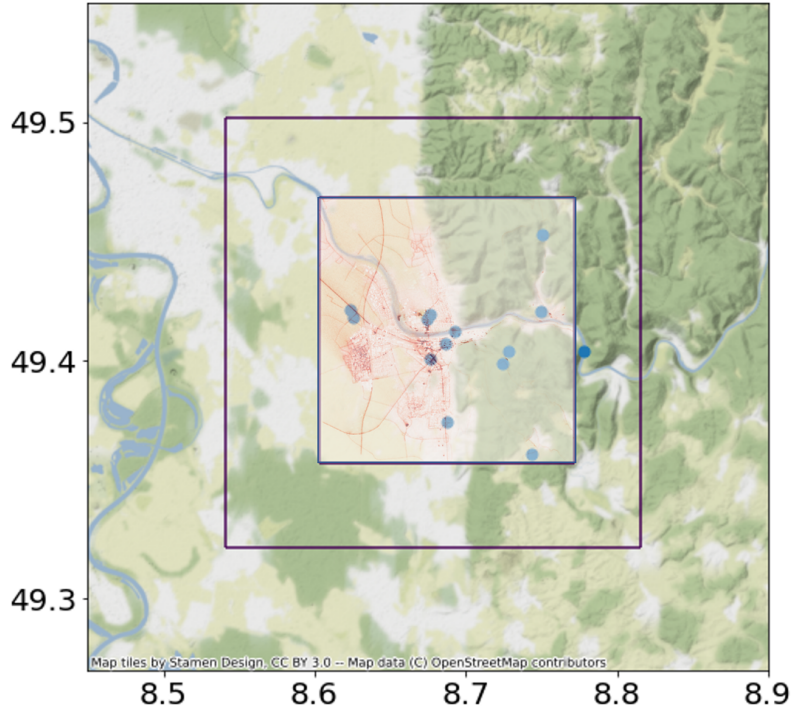
Figure 1. The outer box shows the GRAMM domain, which has an extend of 20 km x 20 km with a resolution of 100 m x 100 m. The inner box shows the GRAL domain with a size of 12.3 km x 12.3 km and a resolution of 10 m x 10 m. Transparently overlayed in the GRAL domain one can see traffic CO_2 enhancement as simulated with GRAL for a specific wind condition. The blue dots denote the meteorological measurement stations for the matching algorithm.

given by the transport model GRAL.

$$y = \mathbf{K}x + \epsilon_y \tag{1}$$

125   with ϵ_y as an vector of length n with Gaussian noise characterising the statistical uncertainty of the measurements. As CO_2 is inert on the timescales on which atmospheric transport in the city takes place, the concentration is proportional to the magnitude of the emissions, which means that the model is linear. The Jacobian matrix $\mathbf{K}$ (m x n) fully describes the linear forward model and scales the concentration fields for each emission group. Each matrix $\mathbf{K}$ for a given meteorological situation is constructed by simulating a concentration field for each emission group x_i with $i \epsilon (1,m)$. The matrix entries $K_{i,j}$ are the

130   sensitivities of concentration of a specific measurement y_j with $j \epsilon (1,n)$ to changes in the emissions of the emission groups:

$$K_{i,j} = \frac{\partial y_j}{\partial x_i} \tag{2}$$

Depending on the emission scenario, a different linear combination of the emission groups forms the total concentration field. As the problem is typically underconstrained and thus, no unique solution exists, regularization is required to obtain a

stable and realistic solution. Therefore, we use a Bayesian inversion approach and constrain the solution x by introducing prior

135   emissions x_a (vector of length m) and prior error covariance $\mathbf{S}_a$ ($m \times m$ matrix) following Rodgers (2000):

$$\hat{x} = x_a + \left(\mathbf{K}^T \mathbf{S}_y^{-1} \mathbf{K} + \mathbf{S}_a^{-1}\right)^{-1} \mathbf{K}^T \mathbf{S}_y^{-1} \left(y - \mathbf{K} x_a\right) \tag{3}$$

The uncertainties in y and $\mathbf{K}$ are assumed to be Gaussian, unbiased, and independent of each other. $\mathbf{S}_y$ ($m \times m$ matrix) denotes

the measurement covariance matrix, which we adjust within the OSSE (see Sect. 3.1). It contains instrument, model and

representation errors. We assume that the matrix $\mathbf{S}_y$ is diagonal implying that the model and measurement errors are not

140   correlated in time and space.

The posterior covariance $\mathbf{S}_{\hat{x}}$ ($n \times n$ matrix) is then given as:

$$\mathbf{S}_{\hat{x}} = (\mathbf{K}^T \mathbf{S}_y^{-1} \mathbf{K} + \mathbf{S}_a^{-1})^{-1}. \tag{4}$$

For derivation see Rodgers (2000).

For multiple time steps, we chain the different atmospheric transport situations by concatenating the matrix $\mathbf{K}$ for each time

145   step t of $t \,\epsilon\, (t_1, ..., t_n)$ and construct a forward model $\mathbf{K}_T$ for all time steps, which can be separated into t_n independent sets of

linear equations if no correlation between states is assumed. The matrices $\mathbf{K}$ for each time step are on the diagonal of the new

matrix $\mathbf{K}_T$ as the model GRAMM/GRAL assumes steady-state conditions. This means that the concentration field in an hour

depends only on the emissions of the respective hour and not on the hours before. If the atmospheric transport changes from

one hour to the next, so will the matrix $\mathbf{K}$.

150

$$\begin{pmatrix} \mathbf{y}_0 \\ \mathbf{y}_1 \\ \vdots \\ \mathbf{y}_{t_n} \end{pmatrix} = \begin{pmatrix} \mathbf{K}_0 & \mathbf{0} & \dots & \mathbf{0} \\ \mathbf{0} & \mathbf{K}_1 & \dots & \mathbf{0} \\ \vdots & \vdots & \ddots & \vdots \\ \mathbf{0} & \mathbf{0} & \dots & \mathbf{K}_{t_n} \end{pmatrix} \cdot \begin{pmatrix} \mathbf{x}_0 \\ \mathbf{x}_1 \\ \vdots \\ \mathbf{x}_{t_n} \end{pmatrix} = \mathbf{K}_T \cdot \begin{pmatrix} \mathbf{x}_0 \\ \mathbf{x}_1 \\ \vdots \\ \mathbf{x}_{t_n} \end{pmatrix}. \tag{5}$$

This equations simplifies and the number of state vectors decreases, if we assume a constant diurnal cycle of the emissions:

$$\begin{pmatrix} \mathbf{y}_0 \\ \mathbf{y}_1 \\ \vdots \\ \mathbf{y}_{23} \\ \mathbf{y}_{24} \\ \mathbf{y}_{25} \\ \vdots \\ \mathbf{y}_{t_n} \end{pmatrix} = \begin{pmatrix} \mathbf{K}_0 & \mathbf{0} & \dots & \mathbf{0} \\ \mathbf{0} & \mathbf{K}_1 & \dots & \mathbf{0} \\ \vdots & \vdots & \ddots & \vdots \\ \mathbf{0} & \mathbf{0} & \dots & \mathbf{K}_{23} \\ \mathbf{K}_{24} & \mathbf{0} & \dots & \mathbf{0} \\ \mathbf{0} & \mathbf{K}_{25} & \dots & \mathbf{0} \\ \vdots & \vdots & \ddots & \vdots \\ \mathbf{0} & \mathbf{0} & \dots & \mathbf{K}_{t_n} \end{pmatrix} \cdot \begin{pmatrix} \mathbf{x}_0 \\ \mathbf{x}_1 \\ \vdots \\ \mathbf{x}_{23} \end{pmatrix} = \mathbf{K}_T \cdot \begin{pmatrix} \mathbf{x}_0 \\ \mathbf{x}_1 \\ \vdots \\ \mathbf{x}_{23} \end{pmatrix} \tag{6}$$

Solving for the posterior emissions $\hat{x}$ requires the prior probability distribution, which is given as a multivariate Gaussian

distribution defined by the vector of the mean values for each state x_a and the covariance matrix $\mathbf{S}_a$. In the case of uncorrelated

states, the prior covariance matrix is $\mathbf{S}_a = \mathbf{diag}(\sigma_a^2)$ with the variances of the state σ_a^2 on the diagonal. For correlated states, a common choice of correlation is an exponentially decaying correlation defined by a single parameter per dimension (Kunik et al., 2019). The single parameter defines the strength of the correlation along a distance of a dimension. In principle, the correlation in the prior reduces the total uncertainty of the prior and links the different hours of the inversion making the inverse problem numerically more complex at the same time. We analyse the influence of temporal correlation in the prior of fluxes in Sec. 3.4. The correlation is defined by a correlation strength τ_t for the time difference between states at the same position. With that the covariance is

$$\mathbf{Cov}(\mathbf{x}_{i,t_0}, \mathbf{x}_{i,t_1}) = \sigma_{i,t_0}\sigma_{i,t_1}\exp\left(\frac{|t_1 - t_0|}{\tau_t}\right) \tag{7}$$

with the standard deviation of state x_i at time t_0 and time t_1 as σ_{i,t_0} and σ_{i,t_1} respectively.

In section 3.3, we analyse the benefit of measuring CO additionally for estimating CO_2 emissions. We assume that they are both passive tracers and thus share the same forward model matrix $\mathbf{K}$. The CO_2 emissions can then be expressed in terms of the CO emissions as

$$\begin{pmatrix} \mathbf{y}_{CO_2} \\ \mathbf{y}_{CO} \end{pmatrix} = \begin{pmatrix} \mathbf{K} & \mathbf{0} \\ \mathbf{0} & \mathbf{K} \end{pmatrix} \cdot \begin{pmatrix} \mathbf{x}_{CO_2} \\ \mathbf{x}_{CO} \end{pmatrix} = \begin{pmatrix} \mathbf{K} & \mathbf{0} \\ \mathbf{0} & \mathbf{K} \end{pmatrix} \cdot \begin{pmatrix} \mathbf{I}_n \\ \mathbf{A}_{CO} \end{pmatrix} \cdot \mathbf{x}_{CO_2} = \begin{pmatrix} \mathbf{K} \\ \mathbf{K}\mathbf{A}_{CO} \end{pmatrix} \cdot \mathbf{x}_{CO_2} \tag{8}$$

with $\mathbf{A}_{CO}$ as a diagonal matrix with the flux-weighted mean emission factors α_{CO} per sector with

$$\alpha_{CO,i} = \frac{\sum_s x_{i,s}\alpha_{CO,s}}{\sum_s \alpha_{CO,s}} \tag{9}$$

with $x_{i,s}$ as the CO_2 emissions of sector s in flux state vector entry i and $\alpha_{CO,s}$ as the emission factor for sector s. $\sum_s$ is the sum over all sectors. We assume the emission factors to be exact for the optimization in the Bayesian inversion system.

2.3 Evaluation metrics

To describe the properties of the inversion and evaluate the set-ups of the OSSE, we introduce evaluation metrics, namely the information content, the relative improvement and the root mean square error (RMSE). The metrics evaluate the quality of the inversion (result) and pick up slightly different aspects of the evaluation. Some require the true emissions, while others are able to evaluate the quality of the inversion without knowing the truth. Further, the metrics differ in the computational costs. For the analysis, we choose the metric that allows us to best analyse the system and highlight the impact.

First, the information content of the measurement can be derived from the concept of Shannon information, which is similar to the physical entropy (Rodgers, 2000). The Shannon information for the difference of prior and posterior probability for the Bayesian inversion in a linear case and given Gaussian probability distribution is:

$$H = -\frac{1}{2}\log(|\mathbf{S}_{\hat{x}}\mathbf{S}_a^{-1}|) = -\frac{1}{2}\log|\mathbf{I}_n - \mathbf{A}| \tag{10}$$

$\mathbf{A}$ denotes the averaging kernel and $\mathbf{I}_n$ is the identity matrix with dimension n. For details on the concept and derivation see Rodgers (2000). One can see that the information content increases with averaging kernel becoming close to identity. The information content describes the quality of the set-up independently of the actual difference between prior and the truth. It can therefore be used as a measure for the quality of the inversion, in which the truth is not known. As it is a scalar quantity, it is useful for optimising observing systems, as well as characterising and comparing them.

However, in an OSSE, the truth is known, such that the difference between truth and posterior emissions can also be used for evaluation of the set-up. The RMSE over the entire domain is defined as the difference between the sum of the two vectors $\hat{x}_{tot}$ and x^*_{tot}.

$$\mathrm{RMSE}(\hat{\mathbf{x}}_{tot}, \mathbf{x}^*_{tot}) = \sqrt{\frac{1}{t_n} \sum_{t=0}^{t_n} \left(\hat{\mathbf{x}}_{tot,t} - \mathbf{x}^*_{tot,t} \right)^2} \tag{11}$$

The RMSE of the total fluxes gives quantitative information on how close the total posterior flux $\hat{x}_{tot}$ is to the true total x^*_{tot} in the domain. In contrast to the information content, it does not capture the complete probability distribution, but rather the effect of the stochastically generated noise. However, it is computationally cheaper to calculate. Additionally, the relative improvement can be calculated, if the true emissions are known:

$$\eta = 1 - \frac{\|\hat{x} - x^*\|_2}{\|x_a - x^*\|_2} \tag{12}$$

with the prior flux x_a, the posterior flux $\hat{x}$, and the true emissions x^*. The relative improvement scales the difference between the posterior and the truth of each state by the difference between the prior and the truth of the states. The relative improvement is 0 % if the RMSE of the posterior has not improved compared to the prior and 100 % if the posterior and the truth are identical.

2.4 Emission data and uncertainties

In this study, we simulate anthropogenic CO_2 enhancements. In the following, we explain the data sets used to construct the true emissions as well as the prior for the inversion. The fluxes of the inventories have a high resolution (see Sect 2.4.1 and 2.4.2), but we group the fluxes into emission groups, which we use as basis vector for the inversion. The emission groups are administrative districts. Therefore, only the total emissions per administrative district is optimised for, even though a district still exhibits a higher resolution sub-structure. While there are actually 26 administrative districts, small districts and districts at the domain border have been aggregated (see Fig. B1) such that there are 19 districts, which can be optimized. To assign area emissions on district level, area sources are interpolated to the GRAL grid of 10 m x 10 m and each pixel on the GRAL grid is assigned to the district with the maximum overlap.

2.4.1 True emissions

For the true emissions, we use data with a high spatial and temporal resolution to reflect the expected heterogeneity and variability of the emissions in the urban area. Traffic emissions were taken from a OpenStreetMap-based emission estimate

(Ulrich et al., 2023) as line sources with street-resolving (3 m) resolution. Combustion emissions are based on data for the yearly consumption of natural gas, fuel, oil, liquid gas, coal, wood and pellets in the municipality of Heidelberg, as provided by the public utility company of Heidelberg. The combustion data is aggregated on a grid with a resolution of 100 m x 100 m to protect the privacy of the customers. For the same reason, if there are less than five customers in a single grid cell, the data is masked and not available in the inventory. We treat masked emissions as if they do not contribute, i.e. set these grid cells to zero. Finally, TNO area emissions from GNFR sector G to L are additionally accounted for as true emissions. However, these area emissions contribute to only 1.4 % to total emissions (see Tab. 1). All true emissions are then cut into administrative districts for division into base vectors, but still have a sub-structure, as described above and as illustrated in Fig. 2.

There are only two TNO point sources in the GRAL domain which are treated each as individual groups. The two TNO point sources in the domain are emitted as point sources at stack heights of 85 m and 120 m. A fixed diurnal and weekly cycle of emissions is assumed following the profiles listed for each GNFR sector by Van Der Gon et al. (2011).

2.4.2 Prior Emissions

We use emission data from the TNO inventory (Super et al., 2020) as starting point for constructing the prior. The data set consists of an inventory of area sources with a resolution of $1/60°$ longitude x $1/120°$ latitude (≈ 1 km x 1 km over Central Europe) and point sources. TNO emissions are shown for the Heidelberg GRAL domain in Fig. A1. While the data set consists of ten different emission maps which were constructed with a Monte-Carlo approach, only the first realization of the set is used. Emissions are divided into emission categories according to the Gridded Nomenclature for Reporting (GNFR) category for both CO_2 and CO. From this, the mean emission factor CO/CO_2 for each GNFR category for the entire GRAL domain is obtained. The emissions and ratios for the Heidelberg domain are listed in Tab.1 and are used in Sec. 2.4.

TNO area emissions are divided into administrative districts as described above. We further smooth out the area TNO emissions such that the mean emissions per area are equal for each district, however they are not constant over the domain as emissions per area still exhibit a sub-structure within the district. The prior emissions are set constant in time and do not have a diurnal cycle. The reason for introducing smoothing across districts, as well as the constant temporal profile for the prior is to reflect a realistic difference between prior and truth that would also be expected in a real inversion. In addition to the area sources, the TNO point sources are also accounted for in the prior.

As an uncertainty for the prior, the standard deviation for the TNO point sources and the smoothed area sources is set to 100 % of the prior flux. As the prior emissions for the traffic and combustion sources are zero, it would prevent the inversion to adjust these fluxes if we used entirely relative uncertainties. Therefore, uncertainties are set to 100 % of the true emissions for traffic and combustion sector.

In total, there are 59 emission groups consisting of two point sources, and 19 districts from the TNO area sources, the traffic simulations, and the combustion data. This choice of emission groups defines the dimension n of the inversion framework. Fig. 2 illustrates the three emission groups (area, combustion and traffic) belonging to the district Weststadt. The emission of all state vector entries is illustrated in Fig. 3 for prior, prior uncertainty and truth.

Table 1. CO_2 and CO emissions per year in Heidelberg and ratio of CO/CO_2 for different GNFR emission sectors as taken from TNO (Super et al., 2020).

GFNR	Sector name	CO_2 emissions [kg/a]	CO emissions [kg/a]	CO/CO_2 [ppb ppm^{-1}]
A	Public Power	1.41e+08	2.76e+05	1.2
B	Industry	5.41e+08	9.64e+05	1.1
C	Fugitives	3.47e+08	1.97e+06	3.6
D	Solvents	0.00e+00	0.00e+00	NaN
E	Road Transport diesel	5.53e+06	3.01e+04	3.5
F1	Road Transport gasoline	6.62e+07	1.07e+06	10.2
F2	Road Transport diesel	1.17e+08	8.68e+04	0.5
F3	Road Transport gas	2.22e+06	6.79e+03	1.9
G	Shipping	7.37e+05	1.23e+03	1.1
H	Aviation	0.00e+00	0.00e+00	NaN
I	OffRoad	6.56e+06	2.34e+05	22.6
J	Waste	0.00e+00	1.78e+02	NaN
L	Agriculture Other	1.01e-07	0.00e+00	0.00e+00

Note the differences between the magnitude of the emission groups in prior and truth. As prior and true emissions are accounted for in different emission groups, corresponding to different vector entries in state x, the inversion needs to redistribute to the other source types to correctly estimate sectoral and spatial patterns. This configuration pushes the limits and tests the capabilities of the inversion system to identify spatially overlapping emission groups. For the entire domain, prior and true emissions differ in average by 13.5 % ((truth-prior)/truth).

2.5 The experiments

This study examines the performance and design parameters of a measurement network by combining a high-resolution atmospheric transport model on building-resolving scale with an atmospheric inverse model. The investigation focuses on various aspects to gain initial insights into the capabilities of a monitoring network in Heidelberg. To systematically analyse different parameters of a measurement network, we conduct four separate experiments, each targeting a specific parameter. We analyse the number of sensors vs. the quality of sensors (Sec.3.1), the optimal horizontal sensor placement (Sec. 3.2), the benefit of utilising CO as additional tracer (Sec. 3.3) and the effect of introducing a temporal correlation in the prior error covariance (Sec. 3.4). In all experiments, the virtual sensors, which "sample" the atmospheric trace gas concentrations are placed at ground level (2 m above ground) and positioned such that they form a rectangular grid that covers the domain. Then either all sensors are used or they are sub-sampled from the grid as described for each respective experiment in Sec. 3. The grid is chosen as a first approach to find the optimal sensor placement. The inversions are performed for wind situations during the period of 22.07.2021 to 21.08.2021. For the experiments in Sec. 3.1 - 3.2, 24 random hours are sampled from the first 300 hours of the
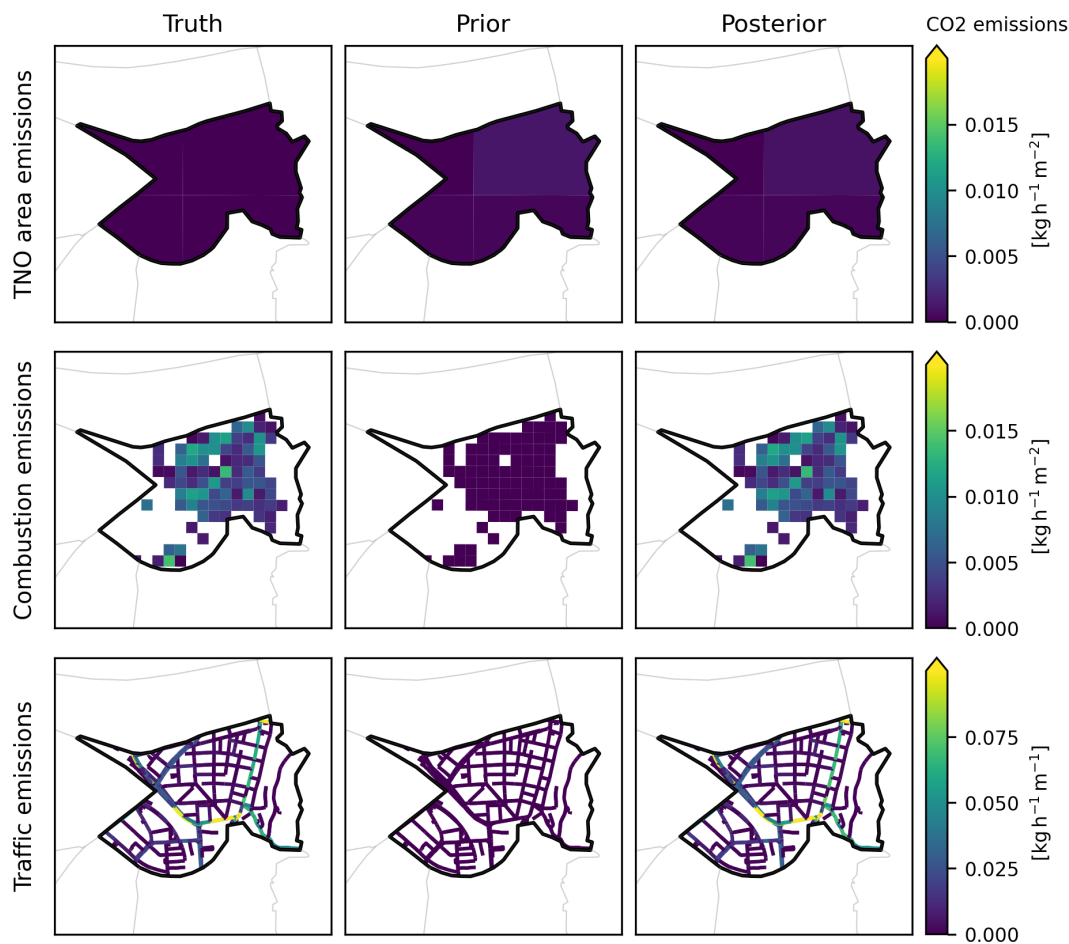
Figure 2. For the city district Weststadt ("We") three elements of the state vector are shown (three rows). The columns show the true, prior and posterior emissions for TNO area emissions (upper row), combustion emissions (middle row) and traffic emissions (lower row). This plot illustrates three of the state entries seen in Fig. 3. Note, that the prior (middle column) for combustion and traffic is zero, but exibits the fixed substructure of the truth. The posterior emissions differ depending on the data assimilated and are illustrated here for 10 CO_2 measurements in the entire Heidelberg domain with 1 ppm uncertainty. Posterior results will be discussed in Sect. 3.

period. For the experiments in Sect. 3.3 - 3.4, the first consecutive 120 hours (5 days) of the period are used for the inversion to test if the posterior estimate captures the correct temporal pattern. For the inversion, we assume constant emissions in Sec. 3.1 - 3.2 and a fixed diurnal cycle as described in Sec. 2.4 for Sec. 3.3 - 3.4. In the conducted OSSE, the influence of biogenic CO_2 fluxes and background concentrations is not considered. Instead, the simulated concentration fields specifically represent the increase in CO_2 concentration resulting from anthropogenic fluxes within the domain. This simplification corresponds to periods when biogenic influences in the city center are very small, most likely in winter, and exact background measurements
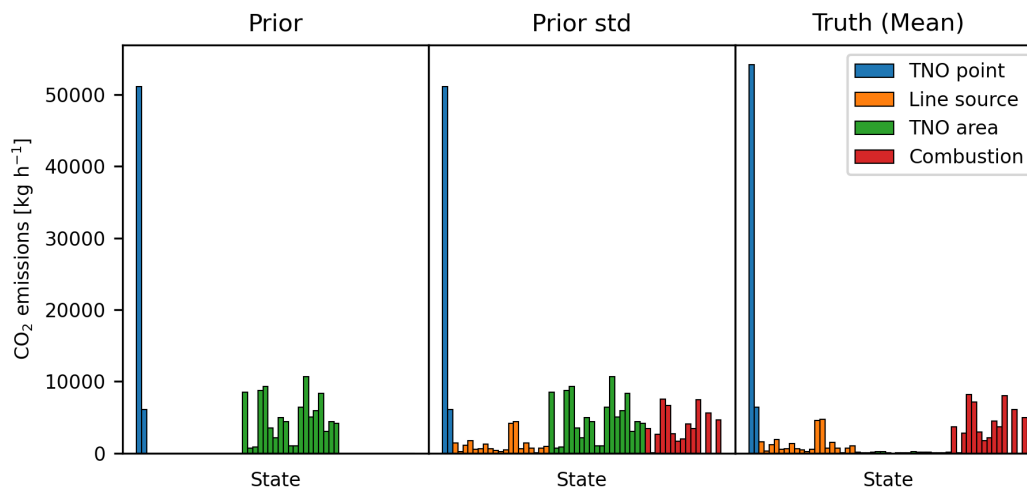
Figure 3. Emissions of each state vector for prior (left), uncertainty of the prior (middle) and truth averaged over time (right). The different emission groups contain emissions from the TNO point (blue) and area sources (green), the traffic simulations (orange), and the combustion sources (red).

are available. Both assumptions are not valid during most parts of the year. However, the goal of this OSSE is to evaluate the inversion framework and analyse the sensitivity of network configurations to CO_2 emission estimates as starting point for optimal network design in Heidelberg. As such, we do not claim completeness.

3 Results

3.1 Sensor quality and quantity

The optimal design of a measurement network is constrained by the total costs of the network limiting quantity and/or quality of the used sensors and transport model. In this experiment, the quality of the inversion is investigated for different numbers of sensors with different mismatch errors $\mathbf{S}_y$. The mismatch error includes instrument errors, model errors as well as representation errors. While all of the errors are inevitable, the instrument errors deserve special focus as it is a design variable for building a monitoring network. High cost sensors have better precision than mid-cost or low cost sensors, but are much more expensive such that we expect a trade-off between quality and quantity for a given budget. We follow the set-up by Turner et al. (2016) and conduct multiple Monte Carlo experiments (each with N = 2000 runs) placing 5, 10, 15, 20, 25 and 30 sensors randomly on a 5 x 6 grid within the domain (30 possible locations) with a total noise of 0.1, 0.5, 1.0, 2.0, 3.0, 4.0, 5.0, 10.0 ppm. We conduct the analysis for 24 randomly selected wind situations. For illustration purposes, Fig. 2 shows the map of the prior, truth and posterior emissions for the three states of area emissions, combustion emission and traffic emissions for the

district of Weststadt in a specific setting (10 CO_2 measurements with 1 ppm uncertainty). The mean posterior result for each state (all districts, all sectors, same setting) can be seen left in Fig. 4.
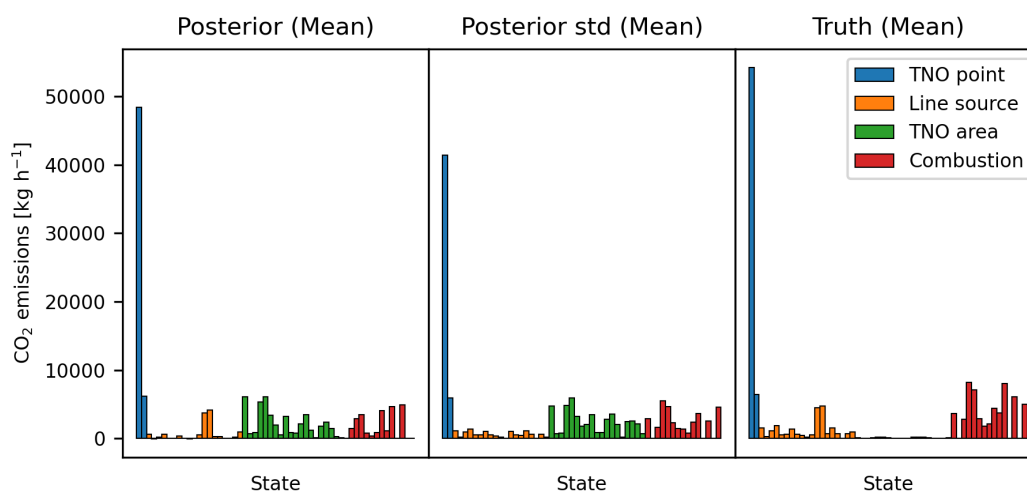
Figure 4. Left: Mean posterior emissions of each state vector. Middle: Mean posterior uncertainty. Right: True emissions of each state vector. The different states refer to emissions from the TNO point (blue) and area sources (green), the traffic simulations (orange), and the combustion sources (red). Note that the prior emissions and uncertainties are given in Fig. 3.

For quantitative analysis of the optimal configuration, Fig. 5 shows the relative improvement of the city-wide emission flux
285 for the different sensor noises and number of sensors. The relative improvement increases with quantity and with decrease of mismatch error, e.g. by increasing the quality of sensors. Similar to Turner et al. (2016), we can identify noise-limited configurations, which improve stronger by increasing the quality of the sensors and models (e.g. 25 sensors at 2 ppm) and site-limited where the increase is stronger for more sensors (e.g. 5 sensors at 2 ppm). The plot now allows comparing the relative improvement for different networks in Heidelberg. This implies, that for any given budget, one can base a decision of
290 investing in more or in better sensors (and models) on these results. Note that we here only account for a random uncertainty in sensor noise assuming uncorrelated measurement uncertainties among sensors. We do not analyse systematic errors within the measurement network, which could be present because of e.g. temperature dependent drifts of the sensors (Delaria et al., 2021) or by a background transport errors. While analyzing systematic offsets was not the scope of this study, the established inverse framework can be easily used to study such effects in future.

295 **3.2 Sensor placement**

In Sect. 3.1 we have randomly sub-sampled a number of sensors from a 5 × 6 grid. Now, we analyse the optimal spatial distribution of the sensors. We therefore compare the sensor placement in a regular grid to randomly selecting locations in the domain. For the random selection, we run Monte Carlo simulations (each N=2000) for different sensor numbers again
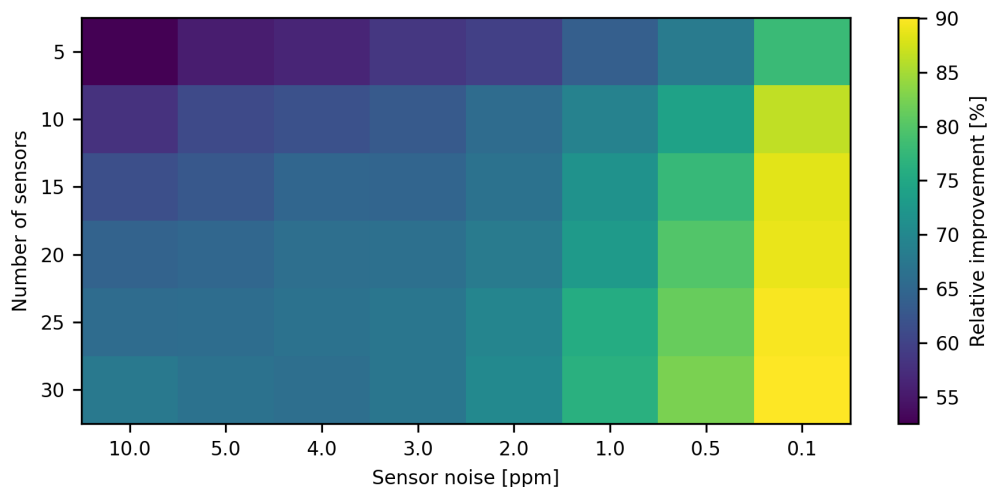
Figure 5. Relative improvement of estimate for different configurations of the number of sensors and the measurement error of the sensors. The relative improvement increases with increasing number of sensors and sensor noise.

using 24 randomly selected wind situations and offering 100 (10 × 10 grid) different possible sensor positions at ground level.

300   We analyse the information content, for 9, 16, and 25 sensors for the random placement and for a regular grid placement assuming a measurement precision of 1 ppm (see Fig. 6). One can clearly see that the information content increases with the number of measurements, as expected as more sensors better inform on the emissions. On average, the grid placement outperforms the random placement as can be seen from the mean values in Fig. 6. This means that without further information on the underlying emission statistics, its benefitial to place the sensors in a regular grid rather than placing them randomly.

305   This is expected as a regular grid covers the entire domain and therefore is less likely to be insensitive to emissions from specific areas. The difference between random and grid placement, as well as the distribution of the random placement, is especially large for a small number of sensors. For a low number of sensors, the random placement of sensors is more likely to be spatially heterogeneous and therefore may be especially well or bad placed contributing to lower and higher information content as in the random placement. The distribution of information content for the random placed samples decreases for

310   higher number of sensors due to a better statistic. Interestingly, the placements with the highest information content are again random placements. We analysed the right tail (10 best performing sensor arrangements) of the random distribution of nine sensors with high information content. Fig. 7 shows the locations of the configurations with the highest information content. The locations with large incident number produce a large information content in many meteorological situations and should therefore be considered as optimal location for a measurement network. As the tail of the distribution corresponds to individual

315   realizations of the Monte-Carlo experiments, it remains unclear whether the "high information content tail" is driven by a specific set of wind situations or if these measurement locations outperform the grid placement in all wind situations. For our Heidelberg setting, one can see that the measurement locations providing most information content are located in the city

center and in vicinity to higher emissions. In the East of the domain, which is dominated by forest areas with low anthropogenic CO_2 emission in the true emissions, only few sensors are placed. In future, we plan to extend this study by considering also

320 measurement stations at higher altitudes above ground as higher stations are less influenced by local sources and are therefore likely to provide information on the emission patterns over a larger area. This might be complementary to the ground-based sensors.
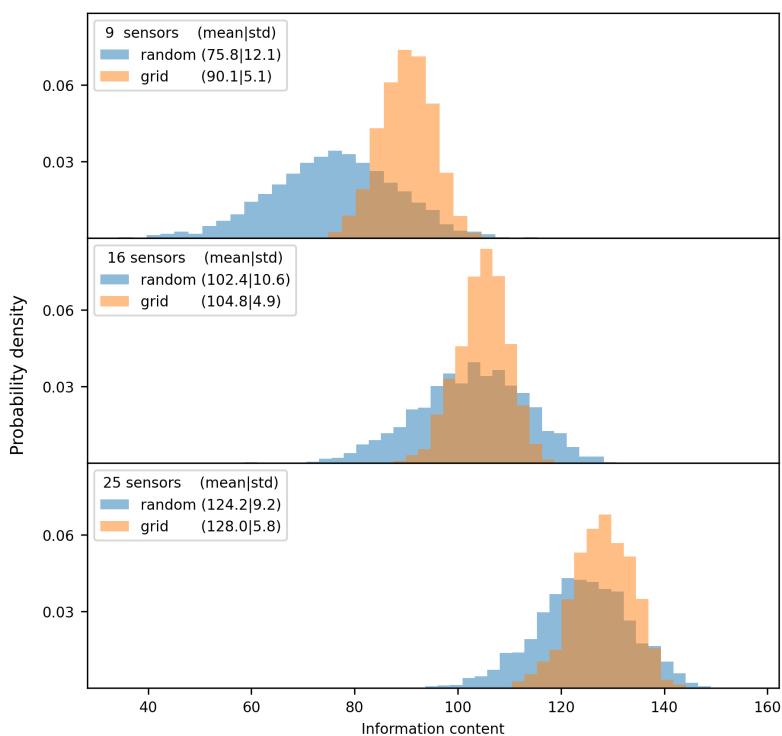
Figure 6. Information content distribution for the inversion set-up for varying wind conditions. The information content increases with number of sensors. The mean information content of randomly placed sensors (blue) is larger in the grid placement, but as the standard deviation of the random placement is larger, the highest information content is achieved for some configurations with randomly placed sensors.

3.3 CO as additional tracer

CO is co-emitted when burning fossil fuels. Depending on the source type, the CO/CO_2 ratio of the emissions differs (see Tab.

325 1). As CO and CO_2 are nearly passive during an hour, both tracers are transported linearly with the same atmospheric transport. Therefore, measuring the atmospheric CO concentration can give additional information about the specific emission groups and potentially also about the total CO_2 emissions in general as both stem from anthropogenic sources. We now analyse to which degree the estimation of CO_2 emissions benefits from measuring CO enhancement as additional tracer alongside CO_2.
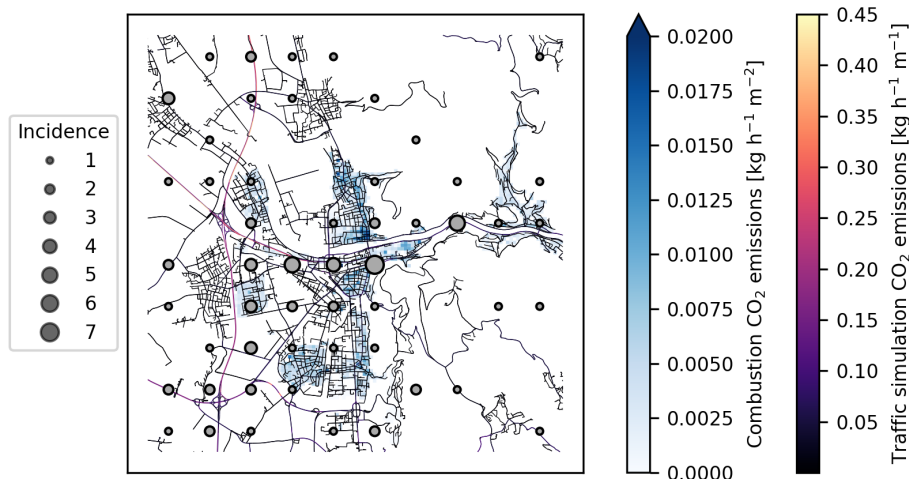
Figure 7. Sensor positions of the 9 sensors with the 10 largest information content. The size of the dots indicates the incidence of the sensor position of the 100 available positions in the experiment.

Note, that we neglect biogenic CO emissions, which are normally expected to be much smaller in cities. While the mean activity ratio of all anthropogenic sources in Heidelberg is $5\,\mathrm{ppb\,ppm^{-1}}$, it is about $16\,\mathrm{ppb\,ppm^{-1}}$ for traffic emissions (see Tab. 1) making CO measurements especially sensitive to traffic emissions.

In this experiment, we assume that all measurement stations measure both CO_2 and CO with uncorrelated measurement errors of $1.0\,\mathrm{ppm}$ for CO_2 and $2.0\,\mathrm{ppb}$ for CO. The inversions are performed for a period of 5 days and the diurnal cycle is assumed to be identical for each day. We conduct this experiment using 10 sensors. The prior is constant during the period and we do not introduce any correlation into the prior.

Fig. 8a shows the total anthropogenic CO_2 emissions during the course of the day. While the prior is constant in time, the truth actually shows a temporal profile with distinct morning peak. One can see that both inversion results (posterior with CO_2 only and with CO_2 and CO) differ from the flat prior and are able to capture the profile of the true emissions. In the given setting, there is no significant improvement of the posterior emissions of total CO_2 when including CO in the inversion. Note that this finding only holds in our setting when neglecting biogenic emissions. However, for future studies, we encourage re-analysing the benefit of CO for total anthropogenic CO_2 when including biogenic emissions. Fig. 8b shows the traffic emissions. Again, both posterior inversions differ from the flat prior emissions. However, the posterior estimate using the CO as additional constraint in the inversion is much closer to the true emissions. The same is true for combustion emissions (see Fig. 8c). This means that in our setting, for given activity ratios and measurement uncertainties, the additional measurement of CO is useful in the inversion to separate different emission groups.
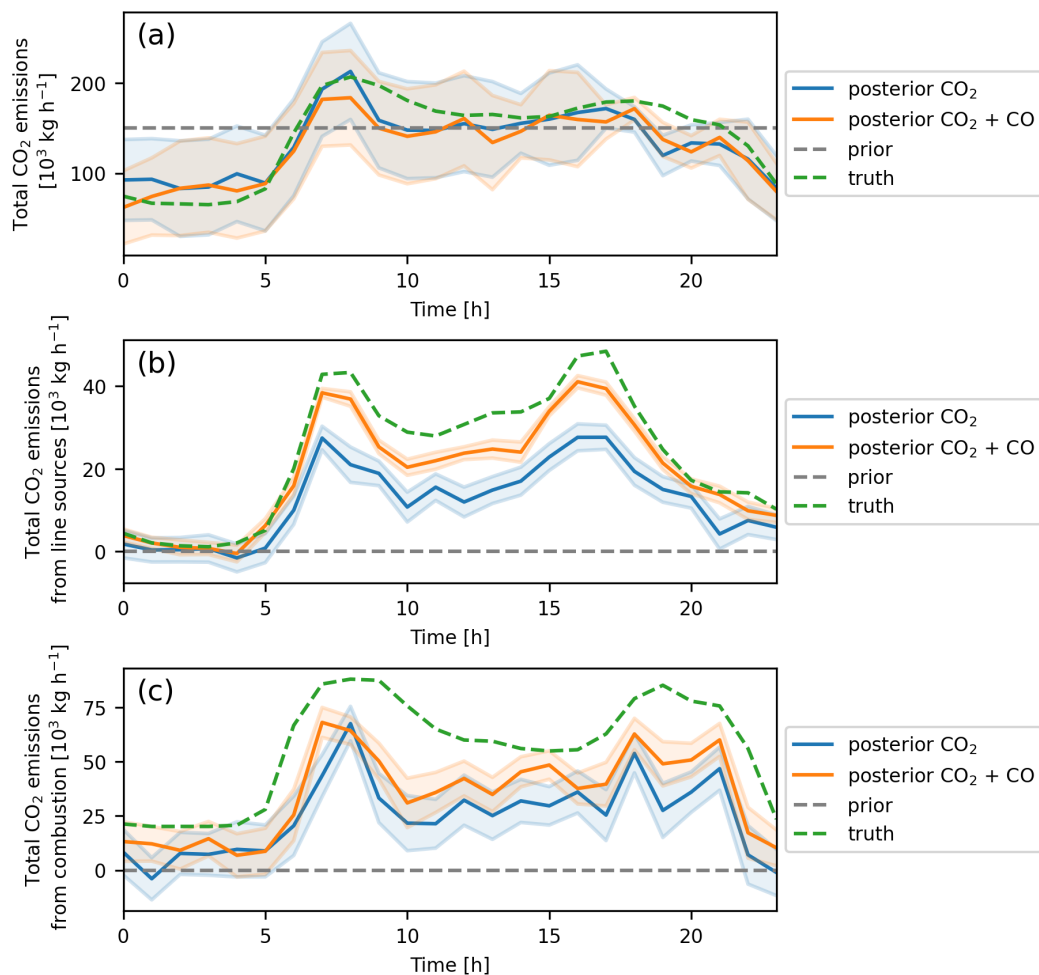
Figure 8. a) Diurnal cycle of the total CO_2 emissions in Heidelberg. The figure shows the posterior for an inversion utilising CO_2 only (blue) and an inversion utilising CO_2 and CO (orange). The shaded area is the standard deviation derived from the posterior covariance. The dotted lines show the prior emissions (gray) and the truth (green. b) Same as a, but for traffic instead of total CO_2 emissions. c) Same as a, but for combustion emissions.

3.4 Temporal correlation of the prior

In the previous sections, we have retrieved the CO_2 emissions for every hour without assuming any correlation between the states. Without temporal correlation, each hour of the inversion is independent of the previous and the following hour. We now examine the effect of considering temporally correlated states. This is appropriate if emissions are correlated such that higher 350 emissions in the past hour are likely to correspond to higher emissions in the following hour. A correlation in the prior reduces the total uncertainty of the prior. However, the choice of the correct correlation length is vital. A larger correlation length leads

to a smoothed time series as measurements inform multiple emission states and thus exhibit a larger corrective power over neighbouring hours. On the other hand, smaller correlation lengths can better account for spikes during the measurements. The choice of optimal correlation length therefore depends on the underlying emission patterns.

355   In a first analysis, we have varied the correlation length τ_h and analysed how the RMSE of the CO_2 emissions for different emission groups change with correlation length (see Fig. 9). This analysis is only possible in an OSSE when the truth is known and a RMSE can actually be determined.
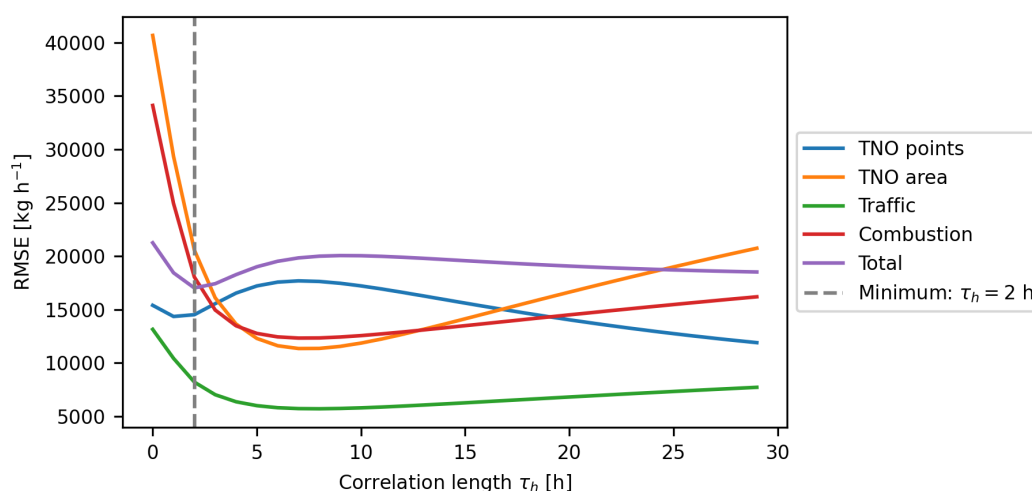
Figure 9. RMSE of the different emission sources for different correlation lengths τ_h. The dashed gray line indicates the minimum of the RMSE for the total emissions, which is at a correlation length of 2 hours.

As the optimal correlation length depends on the temporal emission dynamics, it is dependent on the source type. Focusing on the total CO_2 emissions, we find a clear minimum for about 2 h. It is driven by a shorter optimal correlation length for point 360   sources and longer optimal correlation lengths for traffic, heating or other area emissions. The curve for the point sources, which are emitted at heights of 85 m and 120 m, is qualitatively different from the curve of the ground-based sources. While introducing any correlation time has a positive effect on the RMSE for ground-based sources, the effect can be detrimental for point sources. For point sources, correlation times between 4 and 15 hours are too strong for our setting. We here chose the 2 hours as correlation strength to estimate posterior emissions and highlight the importance of choosing the optimal correlation 365   time especially for determining point sources. In Fig. 10a we analyse the benefit of using a posterior correlation of 2 hours to estimate total CO_2 emissions. The estimation of total CO_2 emissions improves when introducing the prior correlation. While the benefit is only small for total CO_2 emissions, the traffic and combustion emissions improve substantially when introducing a prior correlation (see Fig. 10b and c). This finding for our OSSE in Heidelberg is in accordance with the results from Kunik et al. (2019) in Salt Lake City. It shows that it is beneficial to introduce a temporal correlation of the prior states if underlying 370   emission dynamics are temporally correlated as neighbouring states can inform and correct for each other.
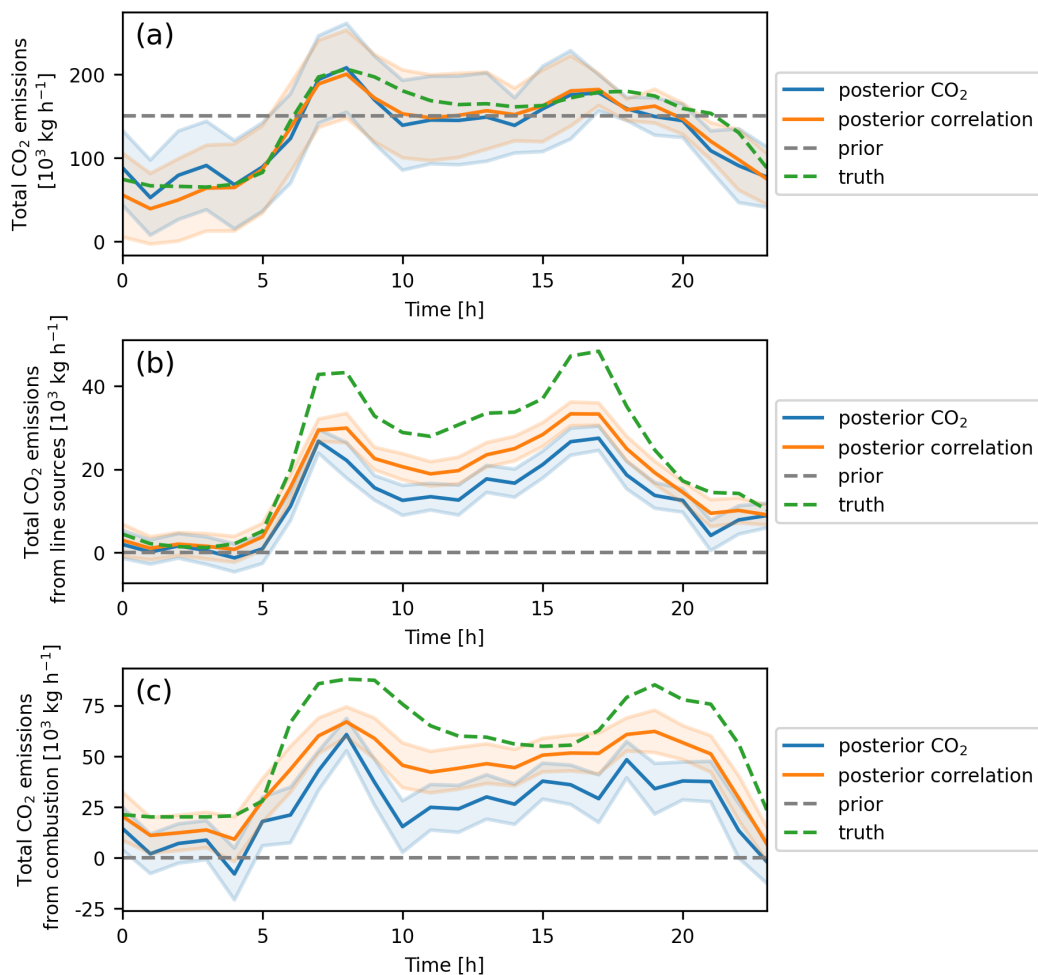
Figure 10. a.) Diurnal cycle of the total CO_2 emissions. The figure shows the posterior for an inversion with uncorrelated prior emissions (blue) and with time correlated prior emissions with a correlation length of two hours (orange). The shaded area is the standard deviation derived from the posterior covariance. The dotted lines show the prior emissions (gray) and the truth (green). b.) Same as a, but for traffic instead of total CO_2 emissions. c.) Same as a, but for combustion CO_2 emissions instead of total CO_2 emissions.

4 Conclusions

We have developed a framework for conducting Observing System Simulation Experiments (OSSE) using the high-resolution transport model GRAMM/GRAL. This framework allows to perform various experiments to assess the capabilities and sensitivity of a measurement network to specific parameters. In the first set of experiments, we investigated the trade-off between sensor quantity and sensor-model quality in the design of a measurement network. The inversion results obtained using the GRAMM/GRAL model qualitatively align with those reported by Turner et al. (2016) showing that there are site-limited and

noise-limited network configurations. Quantitative differences are due to the different underlying emission dynamics and atmospheric conditions in San Francisco and Heidelberg, as well as due to the different resolution of the atmospheric model as well as inverse model used. These experiments determine the trade-off between high-cost and high-quantity sensor networks and

380 provide the basis for selecting an optimal sensor configuration for any given financial budget. While we have only considered statistical noise for the model-data mismatch, the framework allows evaluating systematic biases, e.g. due to sensor drifts.

Next, we analysed the performance of a network with equally spaced sensors versus randomly placed sensors inside the domain. On average, the results demonstrated that equally spaced sensors outperform randomly placed sensors. However, there are certain situations where randomly placed sensors yield better performance, particularly when located near emission

385 sources and in the center of the domain. The GRAMM/GRAL model proves especially advantageous for assessing optimal sensor positions due to the storage of full concentration fields for each wind situation. Other models often compute footprints for pre-defined sites (e.g. Thompson and Pisso (2023)), which makes the analysis of a large number of possible sensor locations less efficient. While we have analysed the concentration fields at ground level, in future we can also elaborate the optimal sensor height above ground level or the optimal mix of sensor heights using the developed inverse framework.

390 We also investigated the impact of CO as an additional tracer in the inversion. While CO measurements do not enhance the estimation of total CO_2 emissions in this specific setting, they significantly improve the estimation of sector-specific emissions. This finding highlights the potential of using CO emissions to differentiate between traffic-related sources and other sources, given that traffic emissions are the primary contributors of CO. The benefits of incorporating CO as an additional tracer for total CO_2 may increase further when biogenic fluxes are considered. As biogenic emissions hardly co-emit CO, using CO as

395 tracer may facilitate separation between anthropogenic and biogenic emissions. Further tracers such as e.g. NO_x, ^{13}C-CO_2 or ^{14}C-CO_2 are also expected to aid estimation of fossil fuel CO_2 (Vardag et al., 2015). Within this developed framework, one can quantify the benefit of including other tracers, each with varying uncertainties and sampling frequencies.

Furthermore, we analysed the influence of the prior probability distribution on the inversion by introducing temporal correlation in the prior emission estimate. The introduction of temporal correlation increases the overall uncertainty reduction. The

400 optimal correlation length is source dependent, but is 2 hours for the total emissions in our setting. Using this correlation length improves the emission estimate and minimises the discrepancy between the posterior emission estimate and the true emissions. Due to the strong improvement when including a temporal correlation, also a spatial correlation length may be included in future.

The developed framework represents a first step towards conducting atmospheric inversions using the transport models with

405 a resolution much below the kilometer scale. The experiments allow comparing different network parameters and therefore optimising the network design based on high-resolution transport. We have demonstrated the feasibility of estimating CO_2 emissions for Heidelberg at a district level and give clear indications for sensor network design. The main advantage of using GRAMM/GRAL in the inversion lies in the cost-effective forward model employed in the catalogue approach, as well as the assumption of hourly steady state in the model. This steady state assumption enables easy determination of the Jacobian re-

410 quired for inversion. This advantageous characteristic facilitates network optimization across various parameters and locations, even encompassing areas influenced by street channeling and buildings. With this framework in place, we can further enhance

the realism of the OSSE by incorporating additional complexities. For instance, introducing biogenic emissions and analysing the effect of background concentrations would be essential for drawing final conclusions on the design of the measurement network in an urban area. Also, the choice of state vectors may be changed from districts with fixed sub-district variation to e.g.

415   a high-resolution grid. This would decrease the aggregation error and account for more realistic spatial dynamics. Numerous additional experiments, such as exploring moving sensors and incorporating additional tracers, are highly desirable and the time period of the inversion can be enlarged. While there are more complexities to be added to the inversion framework, it provides the basis to efficiently estimate high-resolution CO_2 fluxes in an urban setting.

Code and data availability. The inversion code can be found at https://doi.org/10.5281/zenodo.8354902 and https://github.com/ATMO-IUP-
420 UHEI/BayesInverse/tree/v.1.1. Code to read and proccess GRAMM/GRAL output: https://github.com/ATMO-IUP-UHEI/GGpyManager and
https://zenodo.org/record/8375169. Code to conduct the experiments: https://github.com/ATMO-IUP-UHEI/Experiments Forward modelled
concentration data has been simulated using GRAMM/GRAL v19.1 (https://github.com/GralDispersionModel) and is archived on heiData:
https://doi.org/10.11588/data/NHIVDO

Appendix A: Emissions

425 ## A1 Prior emissions
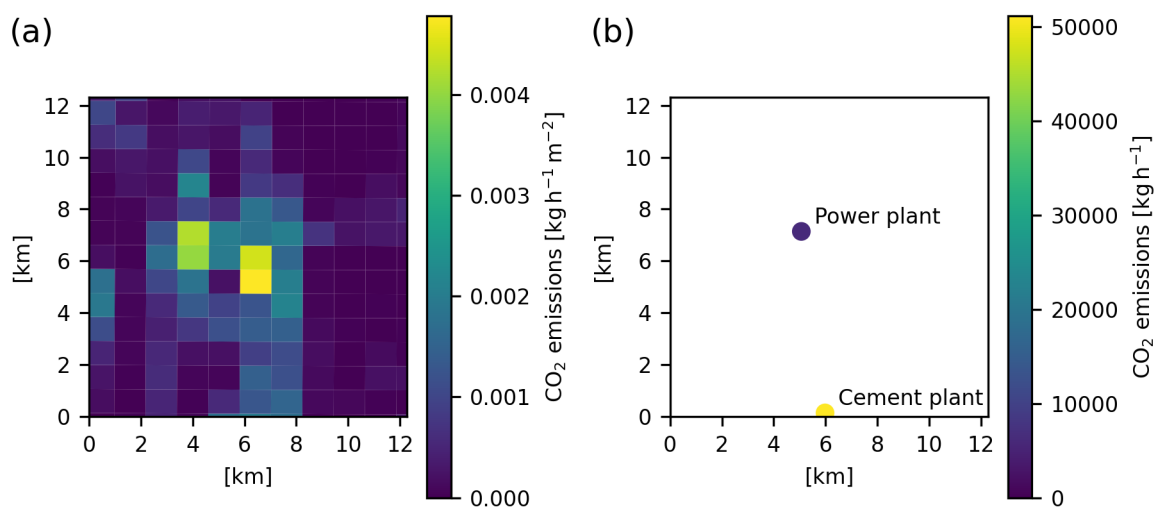
Figure A1. a.): TNO area emissions, b.): TNO point emissions for the GRAL domain in Heidelberg. Data is taken from Super et al. (2020).

Appendix B: Districts chosen as state vectors for the inversion
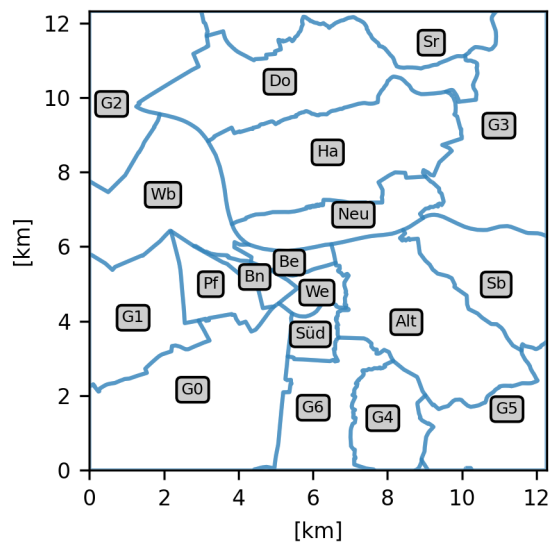
Figure B1. a) The districts used as states for the inversion. The full names as well as the administrative districts inside each district are listed in table B1.

Table B1. Overview over the district names and the administrative districts they represent. Smaller districts or district fragments are grouped together.

Code	Districts	Name
Alt	Altstadt	
Bn	Bahnstadt	
Be	Bergheim	
Do	Dossenheim	
Ha	Handschuhsheim	
Neu	Neuenheim	
Pf	Pfaffengrund	
Sb	Schlierbach	
Sr	Schriesheim	
Süd	Südstadt	
We	Weststadt	
Wb	Wieblingen	
G0	Oftersheim, Kirchheim, Sandhausen	Group 0
G1	Eppelheim, Plankstadt	Group 1
G2	Edingen-Neckarhausen, Ladenburg	Group 2
G3	Schönau, Ziegelhausen, Wilhelmsfeld, Weinheim	Group 3
G4	Emmertsgrund, Boxberg	Group 4
G5	Gaiberg, Bammental, Neckargemünd	Group 5
G6	Leimen, Rohrbach	Group 6

Author contributions. S.N.V conceptualised the experiments, set up the simulations, supervised the work and wrote the the original draft together with R.M. R.M. carried out the formal analysis, performed the simulations and developed the software code.

Competing interests. The authors declare no competing interests.

430 *Acknowledgements.* We thank André Butz for valuable discussions on experimental design and results. We thank Christopher Lueken-Winkels for helpful comments on the final draft. This research was partly funded by the German Research Foundation (DFG) within the Excellence Strategy, ExU 5.2 as granted by the Heidelberg Center for the Environment.

References

Balashov, N. V., Davis, K. J., Miles, N. L., Lauvaux, T., Richardson, S. J., Barkley, Z. R., and Bonin, T. A.: Background heterogeneity and other uncertainties in estimating urban methane flux: results from the Indianapolis Flux Experiment (INFLUX), Atmospheric Chemistry and Physics, 20, 4545–4559, https://doi.org/10.5194/acp-20-4545-2020, publisher: Copernicus GmbH, 2020.

Berchet, A., Zink, K., Muller, C., Oettl, D., Brunner, J., Emmenegger, L., and Brunner, D.: A cost-effective method for simulating city-wide air flow and pollutant dispersion at building resolving scale, Atmospheric Environment, 158, 181–196, https://doi.org/10.1016/j.atmosenv.2017.03.030, publisher: Elsevier Ltd, 2017a.

Berchet, A., Zink, K., Oettl, D., Brunner, J., Emmenegger, L., and Brunner, D.: Evaluation of high-resolution GRAMM–GRAL (v15.12/v14.8) NOx simulations over the city of Zürich, Switzerland, Geoscientific Model Development, 10, 3441–3459, https://doi.org/10.5194/gmd-10-3441-2017, 2017b.

Blocken, B.: LES over RANS in building simulation for outdoor and indoor applications: A foregone conclusion?, Building Simulation, 11, 821–870, https://doi.org/10.1007/s12273-018-0459-3, 2018.

Bréon, F. M., Broquet, G., Puygrenier, V., Chevallier, F., Xueref-Remy, I., Ramonet, M., Dieudonné, E., Lopez, M., Schmidt, M., Perrussel, O., and Ciais, P.: An attempt at estimating Paris area CO2 emissions from atmospheric concentration measurements, Atmospheric Chemistry and Physics, 15, 1707–1724, https://doi.org/10.5194/acp-15-1707-2015, 2015.

Davis, K. J., Deng, A., Lauvaux, T., Miles, N. L., Richardson, S. J., Sarmiento, D. P., Gurney, K. R., Hardesty, R. M., Bonin, T. A., Brewer, W. A., Lamb, B. K., Shepson, P. B., Harvey, R. M., Cambaliza, M. O., Sweeney, C., Turnbull, J. C., Whetstone, J., and Karion, A.: The Indianapolis Flux Experiment (INFLUX): A test-bed for developing urban greenhouse gas emission measurements, Elementa: Science of the Anthropocene, 5, 21, https://doi.org/10.1525/elementa.188, 2017.

Delaria, E. R., Kim, J., Fitzmaurice, H. L., Newman, C., Wooldridge, P. J., Worthington, K., and Cohen, R. C.: The Berkeley Environmental Air-quality and CO_2 Network: field calibrations of sensor temperature dependence and assessment of network scale CO_2 accuracy, Atmospheric Measurement Techniques, 14, 5487–5500, https://doi.org/10.5194/amt-14-5487-2021, publisher: Copernicus GmbH, 2021.

Deng, A., Lauvaux, T., Davis, K. J., Gaudet, B. J., Miles, N., Richardson, S. J., Wu, K., Sarmiento, D. P., Hardesty, R. M., Bonin, T. A., Brewer, W. A., and Gurney, K. R.: Toward reduced transport errors in a high resolution urban CO2 inversion system, Elementa: Science of the Anthropocene, 5, 20, https://doi.org/10.1525/elementa.133, 2017.

Jungmann, M., Vardag, S. N., Kutzner, F., Keppler, F., Schmidt, M., Aeschbach, N., Gerhard, U., Zipf, A., Lautenbach, S., Siegmund, A., Goeschl, T., and Butz, A.: Zooming-in for climate action—hyperlocal greenhouse gas data for mitigation action?, Climate Action, 1, 8, https://doi.org/10.1007/s44168-022-00007-4, 2022.

Kunik, L., Mallia, D. V., Gurney, K. R., Mendoza, D. L., Oda, T., and Lin, J. C.: Bayesian inverse estimation of urban CO2 emissions: Results from a synthetic data simulation over Salt Lake City, UT, Elementa: Science of the Anthropocene, 7, https://doi.org/10.1525/ELEMENTA.375, publisher: University of California Press, 2019.

Lauvaux, T., Miles, N. L., Richardson, S. J., Deng, A., Stauffer, D. R., Davis, K. J., Jacobson, G., Rella, C., Calonder, G.-P., and DeCola, P. L.: Urban Emissions of CO2 from Davos, Switzerland: The First Real-Time Monitoring System Using an Atmospheric Inversion Technique, Journal of Applied Meteorology and Climatology, 52, 2654–2668, https://doi.org/10.1175/JAMC-D-13-038.1, publisher: American Meteorological Society Section: Journal of Applied Meteorology and Climatology, 2013.

Lauvaux, T., Miles, N. L., Deng, A., Richardson, S. J., Cambaliza, M. O., Davis, K. J., Gaudet, B., Gurney, K. R., Huang, J., O'Keefe, D., Song, Y., Karion, A., Oda, T., Patarasuk, R., Razlivanov, I., Sarmiento, D., Shepson, P., Sweeney, C., Turnbull, J., and Wu, K.: High-

470 resolution atmospheric inversion of urban CO2 emissions during the dormant season of the Indianapolis Flux Experiment (INFLUX), Journal of Geophysical Research: Atmospheres, 121, 5213–5236, https://doi.org/10.1002/2015JD024473, 2016.

Lian, J., Lauvaux, T., Utard, H., Bréon, F.-M., Broquet, G., Ramonet, M., Laurent, O., Albarus, I., Cucchi, K., and Ciais, P.: Assessing the Effectiveness of an Urban CO 2 Monitoring Network over the Paris Region through the COVID-19 Lockdown Natural Experiment, Environmental Science & Technology, p. acs.est.1c04973, https://doi.org/10.1021/ACS.EST.1C04973, 2022.

475 Mallia, D. V., Mitchell, L. E., Kunik, L., Fasoli, B., Bares, R., Gurney, K. R., Mendoza, D. L., and Lin, J. C.: Constraining Urban CO2 Emissions Using Mobile Observations from a Light Rail Public Transit Platform, Environmental Science & Technology, 54, 15 613–15 621, https://doi.org/10.1021/acs.est.0c04388, publisher: American Chemical Society, 2020.

Mano, Z., Kendler, S., and Fishbain, B.: Information Theory Solution Approach to the Air Pollution Sensor Location–Allocation Problem, Sensors, 22, 3808, https://doi.org/10.3390/s22103808, number: 10 Publisher: Multidisciplinary Digital Publishing Institute, 2022.

480 Miles, N. L., Davis, K. J., Richardson, S. J., Lauvaux, T., Martins, D. K., Deng, A. J., Balashov, N., Gurney, K. R., Liang, J., Roest, G., Wang, J. A., and Turnbull, J. C.: The influence of near-field fluxes on seasonal carbon dioxide enhancements: results from the Indianapolis Flux Experiment (INFLUX), Carbon Balance and Management, 16, 4, https://doi.org/10.1186/s13021-020-00166-z, 2021.

Nathan, B. J., Lauvaux, T., Turnbull, J. C., Richardson, S. J., Miles, N. L., and Gurney, K. R.: Source Sector Attribution of CO2 Emissions Using an Urban CO/CO2 Bayesian Inversion System, Journal of Geophysical Research: Atmospheres, 123, 13,611–13,621,
485 https://doi.org/10.1029/2018JD029231, 2018.

Oda, T., Lauvaux, T., Lu, D., Rao, P., Miles, N. L., Richardson, S. J., and Gurney, K. R.: On the impact of granularity of space-based urban CO2 emissions in urban atmospheric inversions: A case study for Indianapolis, IN, Elementa: Science of the Anthropocene, 5, 28, https://doi.org/10.1525/elementa.146, 2017.

Oettl, D.: Development of the mesoscale model GRAMM-SCI: Evaluation of simulated highly-resolved flow fields in an alpine and pre-alpine
490 region, Atmosphere, 12, https://doi.org/10.3390/atmos12030298, 2021.

Richardson, S. J., Miles, N. L., Davis, K. J., Lauvaux, T., Martins, D. K., Turnbull, J. C., McKain, K., Sweeney, C., and Cambaliza, M. O. L.: Tower measurement network of in-situ CO2, CH4, and CO in support of the Indianapolis FLUX (INFLUX) Experiment, Elementa: Science of the Anthropocene, 5, 59, https://doi.org/10.1525/elementa.140, 2017.

Rodgers, C. D.: Inverse methods for atmospheric sounding: Theory and practice, vol. 2 of *Series on Atmospheric, Oceanic and Planetary*
495 *Physics*, World Scientific Publishing, 2000.

Super, I., Dellaert, S. N., Visschedijk, A. J., and Van Der Gon, H. A.: Uncertainty analysis of a European high-resolution emission inventory of CO2 and CO to support inverse modelling and network design, Atmospheric Chemistry and Physics, 20, 1795–1816, https://doi.org/10.5194/acp-20-1795-2020, 2020.

Thompson, R. L. and Pisso, I.: A flexible algorithm for network design based on information theory, Atmospheric Measurement Techniques,
500 16, 235–246, https://doi.org/10.5194/amt-16-235-2023, 2023.

Turnbull, J. C., Sweeney, C., Karion, A., Newberger, T., Lehman, S. J., Tans, P. P., Davis, K. J., Lauvaux, T., Miles, N. L., Richardson, S. J., Cambaliza, M. O., Shepson, P. B., Gurney, K., Patarasuk, R., and Razlivanov, I.: Toward quantification and source sector identification of fossil fuel CO2 emissions from an urban area: Results from the INFLUX experiment, Journal of Geophysical Research: Atmospheres, 120, 292–312, https://doi.org/10.1002/2014JD022555, 2015.

505 Turnbull, J. C., Karion, A., Davis, K. J., Lauvaux, T., Miles, N. L., Richardson, S. J., Sweeney, C., McKain, K., Lehman, S. J., Gurney, K. R., Patarasuk, R., Liang, J., Shepson, P. B., Heimburger, A., Harvey, R., and Whetstone, J.: Synthesis of Urban CO2 Emission

Estimates from Multiple Methods from the Indianapolis Flux Project (INFLUX), Environmental Science & Technology, 53, 287–295, https://doi.org/10.1021/acs.est.8b05552, publisher: American Chemical Society, 2019.

Turner, A. J., Shusterman, A. A., McDonald, B. C., Teige, V., Harley, R. A., and Cohen, R. C.: Network design for quantifying urban
510 CO2 emissions: Assessing trade-offs between precision and network density, Atmospheric Chemistry and Physics, 16, 13 465–13 475, https://doi.org/10.5194/acp-16-13465-2016, 2016.

Ulrich, V., Brückner, J., Schultz, M., Vardag, S. N., Ludwig, C., Fürle, J., Zia, M., Lautenbach, S., and Zipf, A.: Private Vehicles Greenhouse Gas Emission Estimation at Street Level for Berlin Based on Open Data, ISPRS International Journal of Geo-Information, 12, 138, https://doi.org/10.3390/ijgi12040138, number: 4 Publisher: Multidisciplinary Digital Publishing Institute, 2023.

515 Van Der Gon, H. D., Hendriks, C., Kuenen, J., Segers, A., and Visschedijk, A.: Description of current temporal emission patterns and sensitivity of predicted AQ for temporal emission patterns., 2011.

Vardag, S. N., Gerbig, C., Janssens-Maenhout, G., and Levin, I.: Estimation of continuous anthropogenic CO2: model-based evaluation of CO2/CO, </sub>, CO, δ13C-CO2 and Δ14C-CO2 tracer methods, Atmospheric Chemistry and Physics, 15, 12 705–12 729, https://doi.org/10.5194/acp-15-12705-2015, 2015.

520 Vogel, F. R., Hammer, S., Steinhof, A., Kromer, B., and Levin, I.: Implication of weekly and diurnal ^{14}C calibration on hourly estimates of CO-based fossil fuel CO_2 ata moderately polluted site in southwestern Germany, Tellus B: Chemical and Physical Meteorology, 62, 512, https://doi.org/10.1111/j.1600-0889.2010.00477.x, 2010.

World Bank: Cities and Climate Change: An Urgent Agenda. Urban development series, Urban Development Series Knowledge Papers, https://openknowledge.worldbank.org/handle/10986/17381, 2010.

525 Wu, K., Lauvaux, T., Davis, K. J., Deng, A., Coto, I. L., Gurney, K. R., and Patarasuk, R.: Joint inverse estimation of fossil fuel and biogenic CO2 fluxes in an urban environment: An observing system simulation experiment to assess the impact of multiple uncertainties, Elementa: Science of the Anthropocene, 6, 17, https://doi.org/10.1525/elementa.138, 2018.

Wu, L., Broquet, G., Ciais, P., Bellassen, V., Vogel, F., Chevallier, F., Xueref-Remy, I., and Wang, Y.: What would dense atmospheric observation networks bring to the quantification of city CO2 emissions?, Atmospheric Chemistry and Physics, 16, 7743–7771,
530 https://doi.org/10.5194/acp-16-7743-2016, 2016.

Öttl, D.: Documentation of the prognostic mesoscale model GRAMM (Graz Mesoscale Model) Vs. 15.12, pp. 1–125, 2020.